Towards 4-photon OAM entanglement experiments

THESIS

submitted in partial fulfillment of the
requirements for the degree of

BACHELOR OF SCIENCE
in
PHYSICS

Author :	C. Bender
Student ID :	s1681036
Supervisor :	Dr. W. Löffler
2^{nd} corrector :	Prof. dr. ir. T. Oosterkamp

Leiden, The Netherlands, July 4, 2019

Towards 4-photon OAM entanglement experiments

C. Bender

Huygens-Kamerlingh Onnes Laboratory, Leiden University
P.O. Box 9500, 2300 RA Leiden, The Netherlands

July 4, 2019

Abstract

We discuss our experimental efforts for generating and measuring four-photon entangled states, entangled in the orbital angular momentum space (OAM). For OAM space photons can be described in a high-dimensional Hilbert space. In order to generate the four-photon states, we use the process of spontaneous parametric down-conversion (SPDC) in a PPKTP crystal. Further a theoretical description on entangled states, Gaussian modes and SPDC is stated.

Contents

Chapter 1

Introduction

At the beginning of the twentieth century the theory of quantum mechanics was introduced. Over the following decades this new physics flourished and became one of the most successful theories of the last century. However, as with most new physical theories, with the rise of quantum theory new problems were exposed. One of these problems was addressed by Einstein, Podolsky and Rosen in 1935 in an elegant thought experiment [1]. They argued that spatially separated entangled particles should be able to somehow interact instantaneous, which would violate the notion that information cannot travel with any speed higher than the speed of light. Later, Schrodinger coined this phenomena as quantum entanglement.

Ever since, a lot of research has been done to this entanglement phenomena and entangled states of a wide variety have been realized experimentally. Systems up to twelve entangled photons have been realized [2], as have bipartite entangled states of increasing dimensionality. However, little research has been done to high-dimensional multipartite entangled states [3, 4].

In this thesis we investigate high-dimensional 4-photon entangled states, realized in their orbital angular momentum (OAM) degrees of freedom. The entangled 4-photon states are generated by use of spontaneous parametric down conversion (SPDC) in a type I PPKTP crystal [5, 6]. For the signal and idler beams we will focus on the fundamental Gaussian mode and the first-order modes in the Laguerre-Gauss and Hermite-Gauss bases [7–9]. First experiments have been explored to measure the coincidence rates of the entangled photons, generated by the SPDC. However further improvements have to be realized in order to better explore the OAM nature of the entangled states. This experiment and its eventual results can

be of interest to application techniques as ghost imaging [10, 11] and secret sharing [12, 13].

We will start this thesis with a description of the required theoretical background, in which we will discuss the fundamentals of quantum states and entanglement, the physics of Gaussian modes and the theory of spontaneous parametric down-conversion. This will be followed by a description of our setup and a discussion of the alignment procedure used. Finally we will state and discuss our first results.

Chapter 2

Quantum States

In this chapter the fundamentals of quantum states will be treated and will be used to describe the concepts of quantum entanglement.

2.1 Dirac Notation

As is convention in quantum theory, we will describe quantum states as state vectors using the Dirac -or bracket notation. In the Dirac notation, there is a clear distinction between a vector and its covector. Vector are denoted by ket vectors, e.g. $|\phi\rangle$. These kets span the ket space. Their covectors, which span its dual vector space (the bra space), are denoted by bra vectors, e.g. $\langle\phi|$. The origin will be denoted by the null vector $|null\rangle$. A one-to-one correspondence exist between the vectors and their covectors [14, Ch. 1]:

$$|\phi\rangle = \alpha\,|\phi_1\rangle + \beta\,|\phi_2\rangle \tag{2.1a}$$

$$\langle\phi| = \alpha^*\,\langle\phi_1| + \beta^*\,\langle\phi_2|\,, \tag{2.1b}$$

where α^* and β^* are the complex conjugate of α and β respectively.

2.2 Hilbert Spaces

The realm of quantum theory is described very successfully with the use of the theory of Hilbert spaces, according to which quantum systems are mathematically described by a specific set of linear vector spaces, i.e. Hilbert Spaces, and the constituents of the system as vectors in such space. In this section we will built up to a mathematical description of Hilbert spaces [15, Ch. 1, 3].

Definition 2.2.1 (Inner Product) *Let V be a linear complex vector space. A transformation $\langle\phi|\psi\rangle$ that maps $V \times V \to \mathbb{C}$, is an inner product (or bracket) in V if for any $|\phi\rangle, |\psi\rangle, |\chi\rangle \in V$ and $\alpha, \beta \in \mathbb{C}$:*

i $\langle\phi|\psi\rangle = \langle\psi|\phi\rangle^*$

ii $\langle\phi|\alpha\psi + \beta\chi\rangle = \alpha\langle\phi|\psi\rangle + \beta\langle\phi|\chi\rangle$

iii $\langle\phi|\phi\rangle \geq 0$

iv $\langle\phi|\phi\rangle = 0$, *if* $|\phi\rangle = |null\rangle$

From *i* and *ii* it follows that the inner product is antilinear in its first argument:

$$\langle\alpha\phi + \beta\psi|\chi\rangle = \alpha^*\langle\phi|\chi\rangle + \beta^*\langle\psi|\chi\rangle \tag{2.2}$$

Every linear complex vector space, which possesses a inner product as defined in definition 2.2.1, is called an inner product space. In an inner product space the following theorems hold.

Theorem 2.2.1 (Inner Product Norm) *For every inner product space V a norm is defined as $\|\phi\| \equiv \||\phi\rangle\| = \langle\phi|\phi\rangle$ and obeys the following properties for $|\phi\rangle, |\psi\rangle \in V$ and $\alpha \in \mathbb{C}$:*

i $\|\phi\| \geq 0$

ii $\|\phi\| = 0, if\ |\phi\rangle = |null\rangle$

iii $\|\alpha\phi\| = |\alpha|\,\|\phi\|$

Theorem 2.2.2 (Schwarzs Inequality) *For $|\phi\rangle, |\psi\rangle \in V$, with V an inner product space,*

$$|\langle\phi|\psi\rangle| \leq \|\phi\|\,\|\psi\|,$$

where $|\langle\phi|\psi\rangle| = \|\phi\|\,\|\psi\|$ only holds if $|\phi\rangle$ and $|\psi\rangle$ are linearly dependent.

Theorem 2.2.3 (Triangle Inequality) *For $|\phi\rangle, |\psi\rangle \in V$, with V an inner product space,*

$$\|\phi + \psi\| \leq \|\phi\| + \|\psi\|$$

Theorem 2.2.4 (Parallelogram Law) *For $|\phi\rangle, |\psi\rangle \in V$, with V an inner product space,*

$$\|\phi + \psi\|^2 + \|\phi - \psi\|^2 = 2(\|\phi\|^2 + \|\psi\|^2)$$

Theorem 2.2.5 (Pythagorean Formula) *For $|\phi\rangle, |\psi\rangle \in V$, with V an inner product space, and $\langle\phi|\psi\rangle = 0$,*

$$\|\phi + \psi\|^2 = \|\phi\|^2 + \|\psi\|^2$$

Being an inner product space is the first prerequisite for being a Hilbert space. Therefore, an inner product space is also termed a pre-Hilbert space. The next property of a Hilbert space is completeness. To define complete, we first have to discuss briefly the meaning of a Cauchy sequence.

Definition 2.2.2 (Cauchy Sequence) *Let $\epsilon \in \mathbb{R}$. Then, a sequence $\{a_n\}_{n=0}^{\infty}$ is said to be a Cauchy sequence if for any $\epsilon > 0$, there exist an $N \in \mathbb{N}$, for which*

$$|a_n - a_m| < \epsilon,$$

with $n, m \geq N$.

Definition 2.2.3 (Completeness) *An inner product space V is said to be complete if every Cauchy sequence $\{a_n\}_{n=0}^{\infty}$ converges to a point in the space V.*

So an inner product space V is complete if there are no holes in V. All points, which can be obtained in V by use of a limit to that point, have to be points in V themselves.

Definition 2.2.4 (Separability) *An inner product space V is said to be separable if it contains a countable, dense subset $\{|\psi_n\rangle\}$. This means that for every $|\phi\rangle \in V$ and every $\epsilon > 0$, with $\epsilon \in \mathbb{R}$, an integer N_ϵ and a set of scalars $\{a_n\}$ exists, for which*

$$\left\| |\phi\rangle - \sum_{n=1}^{N} a_n |\psi_n\rangle \right\| < \epsilon,$$

for $N > N_\epsilon$.

So a subset of V is dense when all points in V can be approached by a combination of members of the subset. Note that def. 2.2.4 does not mean the same as separability of composite states, which will be treated in section 2.4.

With the use of definitions 2.2.1–2.2.4, we can now define a Hilbert space.

Definition 2.2.5 (Hilbert Space) *A complete inner product space which is separable, is called a Hilbert space.*

From now on we will, as is conventional, denote a Hilbert space as $\mathcal{H}$.

2.3 Pure and Mixed States

2.3.1 Density Operator

Another way to describe quantum states, instead of with the use of state vectors, is by working with density operators. This representation has the benefit that it can be used to describe both pure as mixed states (both described below), whereas state vectors can only describe pure states.

Operators are linear transformations that map one vector linearly on another vector in the same Hilbert space and are denoted with a hat, e.g. $\hat{A}$. Operators work on a bra from the right and on a ket from the left, so for an operator $\hat{A} : \mathcal{H} \to \mathcal{H}$ [14, Ch. 1]

$$\langle \phi' | = \langle \phi | \overleftarrow{\hat{A}} \tag{2.3a}$$

$$|\phi'\rangle = \overrightarrow{\hat{A}} |\phi\rangle \equiv |\hat{A}\phi\rangle \tag{2.3b}$$

The adjoint operator is defined as $\langle \hat{A}\phi | \equiv \langle \phi | \hat{A}^\dagger$. Operators can be decomposed using the dyadic product or dyad, e.g. $|u\rangle\langle v|$. The dyadic product is a linear transformation $|u\rangle\langle v| : \mathcal{H} \to \mathcal{H}$, which produces a vector parallel to $|u\rangle$ as [14, Ch. 1]

$$|\phi'\rangle = (|u\rangle\langle v|)\,|\phi\rangle = |u\rangle\,\langle v|\phi\rangle \tag{2.4}$$

In a Hilbert space $\mathcal{H}$ an orthonormal basis can be defined as $\{|i\rangle, i \in \mathbb{N}\}$. Therefore a vector $|\phi\rangle \in \mathcal{H}$ can be decomposed as

$$|\phi\rangle = \sum_i |i\rangle\,\langle i|\phi\rangle = \sum_i (|i\rangle\langle i|)\,|\phi\rangle \tag{2.5}$$

with i ranging up to the dimension of $\mathcal{H}$. Since $|\phi\rangle = \mathbb{1}\,|\phi\rangle$, with $\mathbb{1}$ the identity operator, eq. 2.5 shows that

$$\mathbb{1} = \sum_i |i\rangle\langle i| \tag{2.6}$$

From this we can construct a dyadic decomposition for an arbitrary operator $\hat{A}$

$$\hat{A} = \mathbb{1}\hat{A}\mathbb{1} = \sum_{i,j} |i\rangle\langle i|\,\hat{A}\,|j\rangle\langle j| = \sum_{i,j} \langle i|\hat{A}|j\rangle\,|i\rangle\langle j| = \sum_{i,j} A_{ij}\,|i\rangle\langle j|\,, \tag{2.7}$$

with $A_{ij} = \langle i|\hat{A}|j\rangle$ the matrix elements of $\hat{A}$ and $|i\rangle, |j\rangle$ are the components of the orthonormal basis of $\mathcal{H}$.

A density operator is defined as the dyadic product of a state vector with itself. So for a state, represented by the state vector $|\phi\rangle$, the density operator is defined as [14, Ch. 4]

$$\hat{\rho} \equiv |\phi\rangle\langle\phi| \tag{2.8}$$

As does the state vector, a density operator contains all the statistical information about a quantum state. When measuring a system described by the density operator $\hat{\rho}$, $\langle\psi|\hat{\rho}|\psi\rangle$ can be seen as the probability amplitude of finding the system in state $|\psi\rangle$.

2.3.2 Pure States

A pure state is a quantum state that can be described by a state vector $|\phi\rangle$. These are the kind of states discussed in most introductory quantum text. However, as mentioned earlier, another way of representing pure states is with the use of the density operator. Since the density operator, as defined by eq. 2.8, is composed from its state vector representation $|\phi\rangle$, this definition of the density operator is only valid for pure states. Hence, it is called the density operator of pure states [14, Ch. 4].

For pure states, the density operator has the following properties:

$$\begin{aligned} &(i)\ \hat{\rho}^\dagger = \hat{\rho} \\ &(ii)\ tr(\hat{\rho}) = 1 \\ &(iii)\ \hat{\rho}^2 = \hat{\rho} \end{aligned} \tag{2.9}$$

So for pure states the density operator $\hat{\rho}$ is a Hermitian projection operator. From *ii* and *iii* it follows that $tr(\hat{\rho}^2) = 1$. For an arbitrary operator $\hat{A}$ the expectation value is given by

$$\langle\hat{A}\rangle = tr(\hat{\rho}\hat{A}) \tag{2.10}$$

Qubit Case

The simplest quantum system is the qubit system. A qubit system is a quantum system in a 2-dimensional Hilbert space $\mathcal{H}_2$. A Hilbert space is 2-dimensional if it has no more than two linearly independent sets of states. Qubits are of the general form

$$|\phi\rangle = \alpha\,|0\rangle + \beta\,|1\rangle\,, \tag{2.11}$$

where $\{|0\rangle, |1\rangle\}$ is the orthonormal basis of the Euclidean 2-dimensional Hilbert space and α and β are the statistical weights of the components of the orthonormal basis, with $|\alpha|^2 + |\beta|^2 = 1$. This basis is also referred to as the computational basis*. Some examples of qubit systems are the polarization of photons and the spin projection of the polarization of spin-$\frac{1}{2}$ particles. The density operator of a qubit in the general form of 2.11 then becomes

$$\hat{\rho} = |\phi\rangle\langle\phi| \tag{2.12a}$$
$$= (\alpha|0\rangle + \beta|1\rangle)(\alpha^*\langle 0| + \beta^*\langle 1|) \tag{2.12b}$$
$$= \alpha^2|0\rangle\langle 0| + \alpha\beta^*|0\rangle\langle 1| + \alpha^*\beta|1\rangle\langle 0| + \beta^2|1\rangle\langle 1| \tag{2.12c}$$

As can be seen, although the density operator in eq. 2.12c consist of multiple dyadic terms, it can still be arranged into a single dyadic product (eq. 2.12a and 2.12b) and therefore it describes a pure state.

In the qubit case, the density operator can quite elegantly be visualized using the Bloch sphere. We first have to rewrite the density operator of pure states using the Pauli operators. We now introduce the Pauli operators [14, Ch. 3]:

$$\hat{\sigma}_x = \begin{pmatrix} 0 & 1 \\ 1 & 0 \end{pmatrix} = |0\rangle\langle 1| + |1\rangle\langle 0| \tag{2.13a}$$
$$\hat{\sigma}_y = \begin{pmatrix} 0 & -i \\ i & 0 \end{pmatrix} = -i(|0\rangle\langle 1| - |1\rangle\langle 0|) \tag{2.13b}$$
$$\hat{\sigma}_z = \begin{pmatrix} 1 & 0 \\ 0 & -1 \end{pmatrix} = |0\rangle\langle 0| - |1\rangle\langle 1| \tag{2.13c}$$

The Pauli operators have the following properties, as can be shown from eq. 2.13, with $i, j = x, y, z$:

$$\textit{(i)}\ \ \hat{\sigma}_i^\dagger = \hat{\sigma}_i$$
$$\textit{(ii)}\ \ \hat{\sigma}_i^2 = \mathbb{1} \tag{2.14}$$
$$\textit{(iii)}\ \ tr(\hat{\sigma}_i) = 0$$
$$\textit{(iv)}\ \ [\hat{\sigma}_i, \hat{\sigma}_j] = 2\delta_{ij}\mathbb{1}$$

*For a single qubit the computational basis has no special meaning. So here we just adopt the term as convention.

Version of July 4, 2019– Created July 4, 2019 - 14:30

Here *iv* is equivalent to $tr(\hat{\sigma}_i\hat{\sigma}_j) = 2\delta_{ij}$. The set $\{\frac{1}{\sqrt{2}}\mathbb{1}, \frac{1}{\sqrt{2}}\hat{\sigma}_i\}$ can be seen as an orthonormal operator basis, therefore they can construct any linear operator $\hat{A}$ as [14, Ch. 3]

$$\hat{A} = \frac{1}{2}tr(\hat{A})\mathbb{1} + \frac{1}{2}\sum_{i=1}^{3} tr(\hat{A}\hat{\sigma}_i)\hat{\sigma}_i \tag{2.15}$$

We will denote vectors in the 3-dimensional Euclidean space $\mathbb{R}^3$ by bold letters, e.g. $\mathbf{r}$. We now introduce the Pauli vector operator as $\hat{\boldsymbol{\sigma}} \equiv \hat{\sigma}_x\mathbf{e}_x + \hat{\sigma}_y\mathbf{e}_y + \hat{\sigma}_z\mathbf{e}_z$, where $\mathbf{e}_x$, $\mathbf{e}_y$ and $\mathbf{e}_z$ are the Cartesian orthonormal basis of $\mathbb{R}^3$. From eq. 2.15 and the properties of the pauli operators it is now shown that

$$\hat{\rho} = \frac{1}{2}(\mathbb{1} + \mathbf{r}\hat{\boldsymbol{\sigma}}), \tag{2.16}$$

where $\mathbf{r} \equiv tr(\hat{\rho}\hat{\boldsymbol{\sigma}}) \in \mathbb{R}^3$. Squaring the density operator and taking the trace will then give

$$tr(\hat{\rho}^2) = \frac{1}{4}tr(\mathbb{1} + 2\mathbf{r}\hat{\boldsymbol{\sigma}} + \sum_{i,j} r_i r_j \hat{\sigma}_i\hat{\sigma}_j) \tag{2.17a}$$

$$= \frac{1}{2}(1 + |\mathbf{r}|^2) \tag{2.17b}$$

From the properties *ii* and *iii* of the density operator of pure states we then know that $tr(\hat{\rho}^2) = \frac{1}{2}(1 + |\mathbf{r}|^2) = 1$, and hence $|\mathbf{r}| = 1$. Therefore the qubit case of a pure state is completely defined by $\mathbf{r}$. And since the set of vectors $\{\mathbf{r}\} \in \mathbb{R}^3$ with $|\mathbf{r}| = 1$ can be visualized as points on a spherical surface with radius 1, so can the entire set of 2-dimensional pure states $\{|\phi_n\rangle\}$. This spherical surface is called the Bloch sphere (fig. 2.1).

A unitary transformation on $|\psi\rangle$ according to

$$\left|\psi'\right\rangle = U\left|\psi\right\rangle, \tag{2.18}$$

can be visualized in the Bloch sphere representation by a rotation of $\mathbf{r}$ by an angle φ around the axis $\mathbf{e}$, with [14, Ch. 3]

$$U = R_e(\varphi) = e^{-i\frac{\varphi}{2}\mathbf{e}\hat{\boldsymbol{\sigma}}}, \tag{2.19}$$

where R_e is a rotational transformation around the axis $\mathbf{e}$.

Version of July 4, 2019– Created July 4, 2019 - 14:30

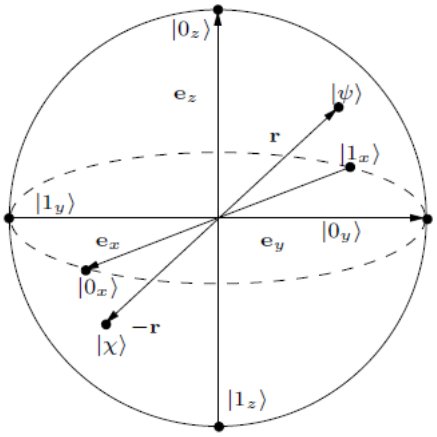

Figure 2.1: *Copied from [14, Fig. 3.1]. The Bloch sphere visualization of a quantum state. $|\psi\rangle$ is visualized by the 3-dimensional vector* $\mathbf{r}$*, with its endpoint lying on the surface of the Bloch sphere, and $|0_i\rangle, |1_i\rangle$, for $i = x, y, z$, are the orthonormal eigenstates of σ_x, σ_y and σ_z, respectively.*

2.3.3 Mixed States

In physical experiments two types of measurements can be categorized: selective measurements, where the preparation procedure is completely determined, and non-selective measurement, where the complete preparation procedure is defined as a weighted superposition of several distinct sub-procedures. In real experiments we mostly encounter non-selective measurements, since systems are often not completely isolated from their surroundings. The distinction between these types of measurements can be best clarified with an example, theretofore we will use the double-slit experiment (fig. 2.2).

In the double-slit experiment a light beam is shot onto a wall containing two slits through which the photons cross and subsequently the photons hit a screen. When the experiment is repeated many times an interference pattern of the incoming photons can be observed. Now assume the photons to be in a state $\hat{\rho}_p$, which is the density operator of pure states as described in eq. 2.8. The slits will act as an operator working on the photon states. Here slit 1 is represented by $\hat{S}_1$ and slit 2 by $\hat{S}_2$ and they transform a photon into a state $\hat{S}_i(\hat{\rho}_p)$, with $i = 1, 2$. Now we also perform a conditional measurement which measures through which slit a photon passes. With the use of this conditional measurement we only collect the data of the photons passing through slit $\hat{S}_1$. This results in photons in state $\hat{S}_1(\hat{\rho}_p)$. This procedure is clearly a selective measurement since we use a

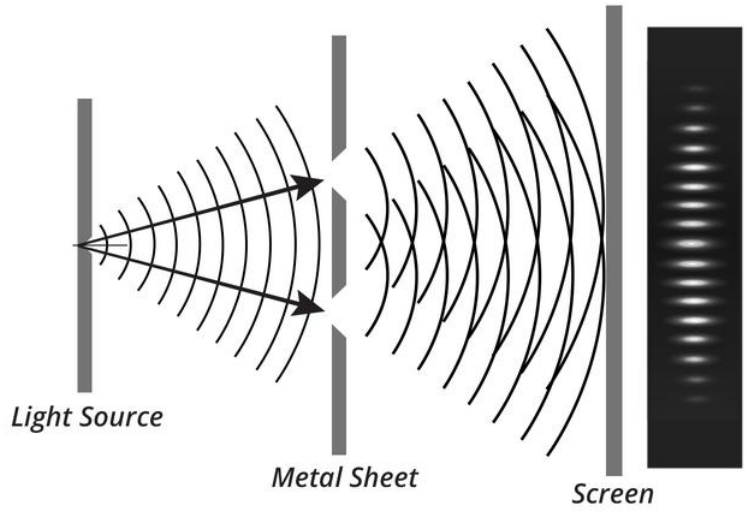

Figure 2.2: *[16] The double-slit experiment. Photons from a light source are shot at sheet with two slits in it. When passing through one of the slits the photon hits a screen. After repeating this process many times an interference pattern appears.*

conditional measurement which completely determines the preparation procedure used on the photons, i.e. $\hat{S}_1$, and it results in a pure state.

When the conditional measurement is omitted the collected data contains information about both the photons that have passed through slit 1 as through slit 2. In this case it is impossible to know through which slit a single photon passed. The photon passes through a slit with some classical probability p_1, p_2, for slit 1 and slit 2 respectively, and $p_1 + p_2 = 1$. The final state prepared by this experiment will be a weighted superposition of the states prepared by the slits separately, and has the form of

$$\hat{\rho}_f = p_1 \hat{S}_1(\hat{\rho}_p) + p_2 \hat{S}_2(\hat{\rho}_p) \tag{2.20}$$

By performing the experiment in such way the preparation procedure is not completely determined, it can be either $\hat{S}_1$ or $\hat{S}_2$. Therefore this is an example of a non-selective measurement. Since the state acquired by this procedure is a superposition of a set of density operators, it cannot be described by a state vector, and it is called a statistical mixture or mixed state. To summarize: selective measurements return pure states, while non-selective measurements return mixed states [14, Ch. 2].

In its general form, the density operator of a mixed state is given by

$$\hat{\rho} \equiv \sum_{i=1}^{N} p_i \left|\phi_i\right\rangle \left\langle\phi_i\right| = \sum_{i=1}^{N} p_i \hat{\rho}_i, \tag{2.21}$$

where $\hat{\rho}_i$ is the density operator of the pure state constituent $|\phi_i\rangle$, N the number of possible preparation procedures and

$$\sum_{i=1}^{N} p_i = 1 \tag{2.22}$$

Further the set of states $\{|\phi_i\rangle\}$ does not have to be orthogonal.

Comparing eq. 2.21 and 2.22 to the properties of the density operator of pure states, we see that the properties *i* and *ii* in eq. 2.9 also hold for the density operator of mixed states. Property *iii* however is not valid for mixed states. For an orthonormal basis $\{|i\rangle\} \in \mathcal{H}$ and coefficients $\{\lambda_i\} \in \mathbb{R}$ a density operator can be composed by

$$\hat{\rho} = \sum_i \lambda_i |i\rangle\langle i| \tag{2.23}$$

By properties *i* and *ii* of eq. 2.9 it can be shown that $\lambda_i = \lambda_i^*, \lambda_i \geq 0$ and $\sum_i \lambda_i = 1$ and therefore

$$0 \leq \lambda_i \leq 1 \tag{2.24}$$

Since the basis $\{|i\rangle\}$ is orthonormal we obtain by squaring the density operator in 2.23

$$\hat{\rho}^2 = \sum_i \lambda_i^2 |i\rangle\langle i| \tag{2.25}$$

By taking the trace this results in

$$tr(\hat{\rho}^2) = \sum_i \lambda_i^2 \leq 1, \tag{2.26}$$

which is equivalent to property *iii* in eq. 2.9 when the equality holds, e.g. a pure state. It also follows that eq. 2.26 has a minimal value of $tr(\hat{\rho}^2) = \frac{1}{d}$, where d is the dimension of $\mathcal{H}$.

Qubit Case

As is done in subsection 2.3.2 for pure states, we will shortly discuss the qubit case for mixed states. Let us first provide a little more clarity on mixed states by giving an example of a mixed qubit state. After which we will complete the Bloch sphere visualization by supplementing the density operators for mixed states to it. For the computational basis $\{|0\rangle, |1\rangle\} \in \mathcal{H}_2$ a mixed qubit state could be

$$\hat{\rho} = \alpha^2 |0\rangle\langle 0| + \beta^2 |1\rangle\langle 1| \tag{2.27}$$

As can be seen it is impossible to decompose this density operator in a single dyadic product of a state vector with itself. The density operator in the example is the sum of the dyadic products $|0\rangle\langle 0|$ and $|1\rangle\langle 1|$ weighted by α^2 and β^2, respectively. Here $|0\rangle\langle 0|$ and $|1\rangle\langle 1|$ can be seen as the pure state density operators of the state vectors $|0\rangle$ and $|1\rangle$, respectively.

Identically to pure states eq. 2.16 can also describe mixed states and therefore

$$tr(\hat{\rho}^2) = \frac{1}{2}(1 + |\mathbf{r}|^2) \tag{2.28}$$

still holds for mixed states. However, since for mixed states $tr(\hat{\rho}^2) \leq 1$ and its minimal value in a 2-dimensional Hilbert space is $tr(\hat{\rho}^2) = \frac{1}{d} = \frac{1}{2}$, we obtain

$$|\mathbf{r}|^2 \leq 1, \tag{2.29}$$

where the equality holds only for pure states. The Bloch sphere visualization can then be completed by stating that pure states can be visualized by vectors having their endpoints on the surface of the sphere and mixed states by vectors having their endpoints in the interior of the sphere. The magnitude of the vector $\mathbf{r}$ can therefore be viewed as the degree of mixture, with $|\mathbf{r}| = 1$ describing a pure state and $|\mathbf{r}| = 0$ describing a maximized statistical mixture.

2.4 Entangled States

A very interesting phenomena in quantum theory is entanglement. Entanglement involves a quantum correlation between particles or states which has no classical resemblance. In this section we will first treat bipartite entangled systems. Subsequently we will built the notion of entanglement to multipartite systems. Following we will discuss a particular example of entanglement, namely the entanglement of orbital angular momentum (OAM), and finally we will consider a process to characterize a system as entangled. Before we start, we first have to present two concepts, tensor products and projective measurements.

Tensor product

A tensor product is a transformation that maps a pair of vectors $(|\phi\rangle, |\psi\rangle)$ of respectively dimensions m, n on a single vector $|\phi\rangle \otimes |\psi\rangle$ of dimension mn. Thus let $\mathcal{H}^i$ be a i-dimensional Hilbert space and let $|\phi\rangle \in \mathcal{H}^m$ and $|\psi\rangle \in \mathcal{H}^n$. A tensor product is a transformation $|\phi\rangle \otimes |\psi\rangle$ that maps $\mathcal{H}^m \otimes$

$\mathcal{H}^n \to \mathcal{H}^{mn}$ according to [17]

$$|\phi\rangle \otimes |\psi\rangle \equiv |\phi,\psi\rangle = \begin{pmatrix} \phi_1 \\ \phi_2 \\ \vdots \\ \phi_m \end{pmatrix} \otimes \begin{pmatrix} \psi_1 \\ \psi_2 \\ \vdots \\ \psi_n \end{pmatrix} = \begin{pmatrix} \phi_1\psi_1 \\ \phi_1\psi_2 \\ \vdots \\ \phi_1\psi_n \\ \phi_2\psi_1 \\ \vdots \\ \phi_m\psi_n \end{pmatrix}, \tag{2.30}$$

where ϕ_i and ψ_i are the ith component of $|\phi\rangle$ and $|\psi\rangle$, respectively.

Projective Measurements

A projective measurement consists of a set of projectors $\{\hat{P}_k\}$ which objects obey

$$\begin{aligned} &(i)\ \ \hat{P}_k^\dagger = \hat{P}_k \\ &(ii)\ \ \textstyle\sum_k \hat{P}_k = \mathbb{1} \\ &(iii)\ \ \hat{P}_k\hat{P}_{k'} = \delta_{k,k'}\hat{P}_k \end{aligned} \tag{2.31}$$

According to Borns rule, when performing a projective measurement on a state $|\phi\rangle$, the probability amplitude the measurement returning an outcome k, i.e. $Pr[k]$, is given by [17]

$$Pr[k] \equiv \langle\phi|\hat{P}_k|\phi\rangle = \langle\hat{P}_k\rangle \tag{2.32}$$

Generalizing the probability amplitude $Pr[k]$ for mixed states will give

$$Pr[k] \equiv tr(\hat{\rho}\hat{P}_k) \tag{2.33}$$

2.4.1 Entanglement

Bipartite Entanglement

Bipartite systems are systems composed of two subsystems. Composite systems do not have to experience any quantum correlations or entanglement. They can also be completely uncorrelated or experience classical correlations, due to classical communication tools between the subsystems. Composite systems can be described with the use of tensor products.

We will start by treating solely pure states. For example, a composite system which consists of two subsystems A and B, with state vectors $|\phi_A\rangle$ and $|\psi_B\rangle$ respectively, can be described by a state vector $|\eta_{AB}\rangle \in \mathcal{H}_A \otimes \mathcal{H}_B \cong \mathcal{H}_{AB}$, according to [17]

$$|\eta_{AB}\rangle = |\phi_A\rangle \otimes |\psi_B\rangle \equiv |\phi_A, \psi_B\rangle \tag{2.34}$$

Or in density operator form

$$\begin{aligned} \hat{\rho}_{AB} &= (|\phi_A\rangle \otimes |\psi_B\rangle)(\langle\phi_A| \otimes \langle\psi_B|) && \text{(2.35a)} \\ &= |\phi_A\rangle\langle\phi_A| \otimes |\psi_B\rangle\langle\psi_B| && \text{(2.35b)} \\ &= \hat{\rho}_A \otimes \hat{\rho}_B && \text{(2.35c)} \end{aligned}$$

The question arises whether or not this composite system exhibit any correlations. The composite state in eq. 2.34 consists of a single tensor product between two pure states and is therefore said to be separable. All separable pure state composite systems are completely uncorrelated. On the other hand a system that is not separable, i.e. of the form $|\eta_{AB}\rangle \neq |\phi_A\rangle \otimes |\psi_B\rangle$ for any choice of basis, is said to be entangled [18]. These are the only two possibilities for pure states, since pure states cannot be classically correlated. However, how do these correlations show up in an experiment.

If we let a projective measurement $\{\hat{P}_k \otimes \hat{P}_l\}$ work on the subsystem A in the composite state $|\eta\rangle$ given by eq. 2.34, after which we will perform the same projective measurement on subsystem B, the expectation value of the projector $\hat{P}_k \otimes \hat{P}_l$ on the composite system is then given by

$$\begin{aligned} \langle \hat{P}_k \otimes \hat{P}_l \rangle_{AB} &= \big\langle \eta_{AB} \big| (\hat{P}_k \otimes \hat{P}_l) \big| \eta_{AB} \big\rangle && \text{(2.36a)} \\ &= tr[\hat{\rho}_{AB}(\hat{P}_k \otimes \hat{P}_l)] && \text{(2.36b)} \\ &= tr[(\hat{\rho}_A \otimes \hat{\rho}_B)(\hat{P}_k \otimes \hat{P}_l)] && \text{(2.36c)} \\ &= tr(\hat{\rho}_A \hat{P}_k) \cdot tr(\hat{\rho}_B \hat{P}_l) && \text{(2.36d)} \\ &= \langle \hat{P}_k \rangle_A \cdot \langle \hat{P}_l \rangle_B, && \text{(2.36e)} \end{aligned}$$

This shows that if one performs a measurement on subsystem A followed by a measurement of subsystem B, the result of the measurement on subsystem B is not affected by the measurement on subsystem A. Instinctively this makes much sense. When this is the case the composite system is not correlated. However, if we follow the same procedure on the composite system

$$|\zeta_{AB}\rangle = \alpha\, |\phi_A\rangle \otimes |\psi_B\rangle + \beta\, |\chi_A\rangle \otimes |\omega_B\rangle\,, \tag{2.37}$$

for $|\phi_A\rangle, |\chi_A\rangle \in \mathcal{H}_A$ and $|\psi_B\rangle, |\omega_B\rangle \in \mathcal{H}_B$ and with $\alpha^2 + \beta^2 = 1$, we will see that it behaves in a different way and that the projective measurement on the composite system will not results in the product of the projective measurements on the subsystems separately.

Let us now calculate the expectation value $\langle \hat{P}_k \rangle_A$ on subsystem A in the composite system. This wil give

$$\langle \hat{P}_k \rangle_A = tr[|\zeta\rangle\langle\zeta|_{AB} (\hat{P}_k \otimes \mathbb{1})] \tag{2.38a}$$
$$= tr_A[tr_B(|\zeta\rangle\langle\zeta|_{AB})\hat{P}_k] \tag{2.38b}$$
$$= tr_A(\hat{\rho}_A \hat{P}_k), \tag{2.38c}$$

where tr_i is defined as the partial trace over subsystem i and $\hat{\rho}_i$ is the reduced density operator of subsystem i. If we do the same calculation for the expectation value $\langle \hat{P}_l \rangle_B$ on subsystem B, we will get the result $\langle \hat{P}_l \rangle_B = tr_B(\hat{\rho}_B \hat{P}_l)$. If the composite system of state $|\zeta_{AB}\rangle$ would be uncorrelated, the product of these two expectation values would be the expectation value $\langle \hat{P}_k \otimes \hat{P}_l \rangle_{AB}$ of the composite system, however

$$\langle \hat{P}_k \otimes \hat{P}_l \rangle_{AB} = tr[\hat{\rho}_{AB}(\hat{P}_k \otimes \hat{P}_l)] \neq tr_A(\hat{\rho}_A \hat{P}_k) \cdot tr_B(\hat{\rho}_B \hat{P}_l) \tag{2.39}$$

Therefore a measurement on subsystem A will affect a subsequent measurement on subsystem B and vice verse. This means the composite system is correlated and since pure states cannot be classically correlated, the state $|\zeta_{AB}\rangle$ is an entangled state [14, Ch. 8].

We will now generalize the concepts of correlations to include mixed states [18]. Equivalently to pure states, a mixed state composite system is described by a single tensor product of the density operator of its two subsystems A and B as

$$\hat{\rho}_{AB} = \hat{\rho}_A \otimes \hat{\rho}_B \tag{2.40}$$

is completely uncorrelated. Another form in which composite systems of mixed states can be encountered is[†]

$$\hat{\rho}_{AB} = \sum_i p_i \hat{\rho}_i^A \otimes \hat{\rho}_i^B, with m \neq 1, \tag{2.41}$$

where the composite system is described as a weighted superposition of product states, with $p_i \geq 0$ and $\sum_i p_i = 1$. For such a state it holds in general that $tr[\hat{\rho}_{AB}(\hat{P}_k \otimes \hat{P}_l)] \neq tr_A(\hat{\rho}_A \hat{P}_k) \cdot tr_B(\hat{\rho}_B \hat{P}_l)$ and will therefore exhibit correlated measurements. However, since the correlation properties of eq. 2.41 are completely determined by the classical probabilities p_i,

[†]Here we denote the subsystem as superscript, since the iterations of the summation are already denoted as subscript.

such a state is classically correlated and is called a separable mixed state. A clear difference between classical correlated states and entangled states is that a transformation of basis can turn a classically correlated state in a completely uncorrelated state, while entangled state remains entangled independent of the choice of basis [14, Ch. 8]. We define entangled mixed states as a state that cannot be described as a weighted superposition of product states, i.e.

$$\hat{\rho}_{AB} \neq \sum_i p_i \hat{\rho}_i^A \otimes \hat{\rho}_i^B, with m \neq 1 \tag{2.42}$$

Let us now look at a specific example for entanglement of qubits to clarify the kind of correlations we talk about [17]. Let us perform the projective measurement $\{\hat{P}_{j,k} = |j\rangle\langle j| \otimes |k\rangle\langle k|\}$ on the Bell state

$$\left|\Phi^+\right\rangle = \frac{|0\rangle \otimes |0\rangle + |1\rangle \otimes |1\rangle}{\sqrt{2}} \tag{2.43}$$

We can now calculate the probability of returning the possible outcomes of the projective measurement on the state $|\Phi^+\rangle$. Let us start with $Pr[(0,0)]$

$$\begin{aligned} Pr[(0,0)] &= \left\langle\Phi^+\right|\hat{P}_{0,0}\left|\Phi^+\right\rangle && \text{(2.44a)}\\ &= \left\langle\Phi^+\right||0\rangle\langle 0| \otimes |0\rangle\langle 0|\left|\Phi^+\right\rangle && \text{(2.44b)}\\ &= \frac{1}{2}[(\langle 0| \otimes \langle 0|)(|0\rangle\langle 0| \otimes |0\rangle\langle 0|)(|0\rangle \otimes |0\rangle)] && \text{(2.44c)}\\ &= \frac{1}{2} && \text{(2.44d)} \end{aligned}$$

The other three possible projectors of the projective measurement will return the probabilities

$$Pr[(1,1)] = \frac{1}{2}, \quad Pr[(1,0)] = 0, \quad Pr[(0,1)] = 0 \tag{2.45}$$

We can perform the same projective measurement in a different basis. Let us define the basis $\{|+\rangle, |-\rangle\}$, with

$$|+\rangle = \frac{1}{\sqrt{2}}(|0\rangle + |1\rangle), \qquad |-\rangle = \frac{1}{\sqrt{2}}(|0\rangle - |1\rangle) \tag{2.46}$$

In this basis the state $|\Phi^+\rangle$ becomes

$$\left|\Phi^+\right\rangle = \frac{(|+\rangle + |-\rangle) \otimes (|+\rangle + |-\rangle) + (|+\rangle - |-\rangle) \otimes (|+\rangle - |-\rangle)}{2}, \tag{2.47}$$

and for the projector $\hat{P}_{+,+}$ we obtain

$$Pr[(+,+)] = \left\langle \Phi^+ \middle| \hat{P}_{+,+} \middle| \Phi^+ \right\rangle \tag{2.48a}$$
$$= \left\langle \Phi^+ \middle| |+\rangle\langle +| \otimes |+\rangle\langle +| \middle| \Phi^+ \right\rangle \tag{2.48b}$$
$$= \frac{1}{2} \tag{2.48c}$$

For the other projectors we obtain

$$Pr[(-,-)] = \frac{1}{2}, \quad Pr[(+,-)] = 0 \quad Pr[(-,+)] = 0 \tag{2.49}$$

We see that this results in the same perfect correlation. This correlation is obtained in any choice of basis.

Multipartite Entanglement

We have already discussed the notion of entanglement in the case of bipartite systems and as it turns out it is quite straightforward to generalize this to the case of multipartite systems. Here we will just state the generalizations of multipartite systems [19], since the entanglement definitions are highly equivalent with respect to bipartite systems. For multipartite systems we will denote the subsystems with numbers instead of with capital letters, as we did for bipartite systems.

We will start again with pure states. A multipartite system $|\eta_{1\otimes\cdots\otimes N}\rangle \in \mathcal{H}_1 \otimes \cdots \otimes \mathcal{H}_N$, consisting of N subsystems is said to be separable, i.e. completely uncorrelated, if it can be described as

$$|\eta_{1\otimes\cdots\otimes N}\rangle = |\phi_1\rangle \otimes \cdots \otimes |\phi_N\rangle\,, \tag{2.50}$$

where $|\phi_i\rangle$ describes the ith subsystem. This state is separable, since it has only a single term consisting of tensor products. Therefore a measurement on one of the subsystems will not affect measurements on the other subsystems. A pure state multipartite system is said to be entangled if it cannot be written in the form of eq. 2.50. This definition of multipartite entangled systems shows great similarity to the bipartite case.

When considering mixed state composite systems the same similarity arises. Again a completely uncorrelated composite system, consisting of N subsystems, can be described as

$$\hat{\rho}_{1\otimes\cdots\otimes N} = \hat{\rho}_1 \otimes \cdots \otimes \hat{\rho}_N \tag{2.51}$$

A mixed state composite system is classically correlated if it can be described by[‡][19]

$$\hat{\rho}_{1\otimes\cdots\otimes N} = \sum_{i=1} p_i \hat{\rho}_i^{(1)} \otimes \cdots \otimes \hat{\rho}_i^{(N)}, with m \neq 1, \tag{2.52}$$

since these correlations are again completely determined by the classical probabilities p_i. Any multipartite system that cannot be described as a weighted superposition of multipartite product state (eq. 2.52) is entangled. Although the multipartite case is very similar to the bipartite case, rewriting the states in desired form can be quite cumbersome and the entanglement features of the states can be hard to track down.

2.4.2 Schmidt Decomposition and Witness Operator

Since it can be hard to determine whether a composite state is separable or not, we need more straightforward ways to determine this state property. In this section we will discuss such procedures for bipartite systems. We will start with a procedure for pure states, the Schmidt decomposition. After which we will treat the witness operator for mixed states.

Schmidt Decomposition

For two orthonormal bases $\{|\phi_i\rangle\}_A \in \mathcal{H}_A$ and $\{|\psi_i\rangle\}_B \in \mathcal{H}_B$ any pure state $|\eta_{AB}\rangle \in \mathcal{H}_A \otimes \mathcal{H}_B$ can be constructed as

$$|\eta_{AB}\rangle = \sum_{i,j} d_{i,j} |\phi_i\rangle \otimes |\psi_i\rangle \tag{2.53}$$

Also there always exist unitary transformations u and v such that udv is diagonal, with diagonal entries $[udv]_{i,i} = \sqrt{\lambda_i}$ [18]. This basis results in

$$|\eta_{AB}\rangle = \sum_i \sqrt{\lambda_i} \left|\phi_i'\right\rangle \otimes \left|\psi_i'\right\rangle, \tag{2.54}$$

where $\sqrt{\lambda_i}$ are called the Schmidt coefficients. As discussed in section 2.4.1, eq. 2.54 will only describe a separable state if it has only one nonzero Schmidt coefficient. When more then one Schmidt coefficient has a nonzero value, the state $|\eta_{AB}\rangle$ is an entangled state [18]. Since the composite basis

[‡]The subsystems are again denoted with a superscript to not get in the way of the iterations of the summation.

$\left|\phi_i'\right\rangle \otimes \left|\psi_i'\right\rangle$ consists of separable states, all information regarding the entanglement of the state $|\eta_{AB}\rangle$ is determined by the Schmidt coefficients [18].

When we look into the reduced density operator of the subsystems, it can be shown that they can be written as [18]

$$\hat{\rho}_A = \sum_i \lambda_i \left|\phi_i'\right\rangle\langle\phi_i'\right|, \quad \hat{\rho}_B = \sum_i \lambda_i \left|\psi_i'\right\rangle\langle\psi_i'\right| \tag{2.55}$$

As been said, if the Schmidt coefficients have only one nonnegative entry the state is separable. Therefore for separable states the reduced state in eq. 2.55 are pure states, while for entangled states the reduced states are statistical mixtures. So to summarize for pure state composite systems, the composite state is separable if its subsystems are pure states and the composite state is entangled if the subsystems are mixed states.

Witness Operator

For mixed composite states, entanglement properties can be indicated by a witness operator. An operator $\hat{W}$ is a witness operator if it is hermitian and not positive definitive, but gives a nonnegative expectation value [18], i.e.

$$\langle\phi|\hat{W}|\phi\rangle \geq 0, \tag{2.56}$$

for any separable pure state $|\phi\rangle$. However, a separable mixed state can be described by a weighted superposition of density operator of pure states (eq. 2.21). Hence, the expectation value of a witness operator working on any separable mixed state will return

$$tr(\hat{\rho}_s\hat{W}) = \sum_i p_i \langle\phi_i|W|\phi_i\rangle \geq 0 \tag{2.57}$$

Therefore, when a witness operator works on a mixed state density operator $\hat{\rho}_e$ and the expectation value returns

$$tr(\hat{\rho}_e\hat{W}) < 0, \tag{2.58}$$

$\hat{\rho}_e$ has to be entangled. A witness operator can be found for any entangled state.

Version of July 4, 2019– Created July 4, 2019 - 14:30

Chapter 3

Gaussian Modes

3.1 OAM of Light

In quantum theory the angular momentum is split into two components, the orbital angular momentum (OAM) and the spin. The orbital angular momentum is the quantum counterpart of the classical angular momentum, whereas the spin does not have a classical counterpart. In case of the angular momentum of light, the spin can be associated with the polarization of the light field, since its eigenstates are the states of circularly polarization of the paraxial light field [21]. The orbital component of the angular momentum of light can be associated with the spatial distribution of the light field. For light fields carrying a nonzero orbital angular momentum in the paraxial approximation, this results in helical wavefronts

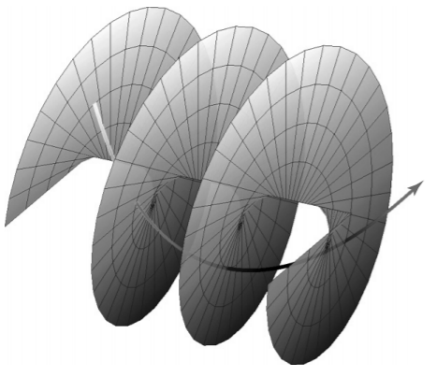

Figure 3.1: *Copied from [21, fig. 1.1] A helical wavefront due to a azimuthal phase with $\ell = 1$. Hence the light beam consists of photons with orbital angular momentum $\ell\hbar$.*

(fig. 3.1), whereas light beams having a zero orbital angular momentum consist of plane or spherical wavefronts. These helical wavefronts are twisting around the propagation axis. The relation between the helical structure of the wavefronts and the orbital angular momentum is captured in the winding number of the helicity ℓ. For a light beam consisting of photons of orbital angular momentum $\ell\hbar$, the wavefronts consists of $|\ell|$ intertwined helices with a spatial period of $\ell\lambda$ [20], where λ is the wavelength of the photons. The handedness of the helicity is given by the sign of ℓ. Since coaxial OAM modes are mutually orthogonal and ℓ can take all integer values, the OAM modes span a high-dimensional Hilbert space [20]. Therefore orbital angular momentum is an appropriate property to explore high-dimensional entangled states. An example of a light mode which exhibits orbital angular momentum features, is the Laguerre-Gauss mode (LG_p^ℓ), which is discussed in the next section.

3.2 Gaussian Modes

In this section we will discuss some examples of OAM modes of light, which are solutions to the paraxial wave equation. We will only look at monochromatic beams. First, we will derive the paraxial wave equation itself. In order to do this we will start with the wave equation

$$\hat{\nabla}^2\mathbf{E} - \frac{1}{c^2}\frac{\partial^2\mathbf{E}}{\partial t^2} = \mathbf{0}, \tag{3.1}$$

where $\mathbf{E}$ is the electric field and c is the speed of light. We can use separation of variable to split the electric field in a spatial component and a temporal component according to [22]

$$\mathbf{E}(x,y,z,t) = u(x,y,z)e^{-i\omega t}\hat{\mathbf{n}}, \tag{3.2}$$

where $u(x,y,z)$ is the spatially dependent amplitude of the electric field and $\hat{\mathbf{n}}$ is the direction of polarization. This results in a wave equation of the form

$$\frac{1}{u(x,y,z)}\hat{\nabla}^2 u(x,y,z) = \frac{1}{c^2 e^{-i\omega t}}\frac{d^2 e^{-i\omega t}}{dt^2} \tag{3.3}$$

Since both sides of the equation depend on different variables, this equation can only be valid if both side of the equation are equal to a constant, which we call $-k^2$. Therefore, inserting the spatial part into the wave equation will give us the Helmholtz equation

$$\hat{\nabla}^2 u + k^2 u = 0 \tag{3.4}$$

For a light beam propagating in the z-direction, we will make the ansatz, that the spatial amplitude $u(x, y, z)$ will be of the form [22]

$$u(x, y, z) = u_0(x, y, z)e^{ikz} \tag{3.5}$$

Inserting this ansatz into the Helmholtz equation will give us

$$\frac{\partial^2 u_0}{\partial x^2} + \frac{\partial^2 u_0}{\partial y^2} + \frac{\partial^2 u_0}{\partial z^2} + 2ik\frac{\partial u_0}{\partial z} = 0 \tag{3.6}$$

Since the electric field of a light beam varies very slowly in the direction of propagation, we know that

$$\left|\frac{\partial^2 u_0}{\partial z^2}\right| \ll \left|\frac{\partial^2 u_0}{\partial x^2}\right|, \left|\frac{\partial^2 u_0}{\partial y^2}\right|, \left|2k\frac{\partial u_0}{\partial z}\right| \tag{3.7}$$

Therefore we can neglect the term of the second derivative with respect to z. By doing this we obtain the paraxial wave equation

$$\frac{\partial^2 u_0}{\partial x^2} + \frac{\partial^2 u_0}{\partial y^2} + 2ik\frac{\partial u_0}{\partial z} = \hat{\nabla}_t^2 + 2ik\frac{\partial u_0}{\partial z} = 0, \tag{3.8}$$

where $\hat{\nabla}_t^2$ is the Laplacian operator working on the transverse space. The paraxial wave equation is the form of the Helmholtz equation, which gives solution describing the electric field with slowly varying z-component, i.e. light beams.

3.2.1 Fundamental Gaussian Mode

One of the most frequently encountered solutions to the paraxial wave equation is the solution of the fundamental Gaussian mode or just Gaussian mode (fig. 3.2). The Gaussian mode can be seen as an OAM mode of light with a zero orbital angular momentum, i.e. $\ell = 0$. Therefore the Gaussian mode does not have a helical wavefront, in fact it has a spherical wavefront [23]. The Gaussian mode is described by a solution of the paraxial wave equation, where the electric field strength in the transverse direction decreases as a Gaussian distribution. Hence we can make an ansatz of the form of the solution of the paraxial wave equation. In this ansatz we separate the x, y-dependency from the z-dependency and we let the x, y-dependency be described by a Gaussian distribution. This results in the form [22]

$$u_0(x, y, z) = Ae^{\frac{ik(x^2+y^2)}{2q(z)}}e^{ip(z)}, \tag{3.9}$$

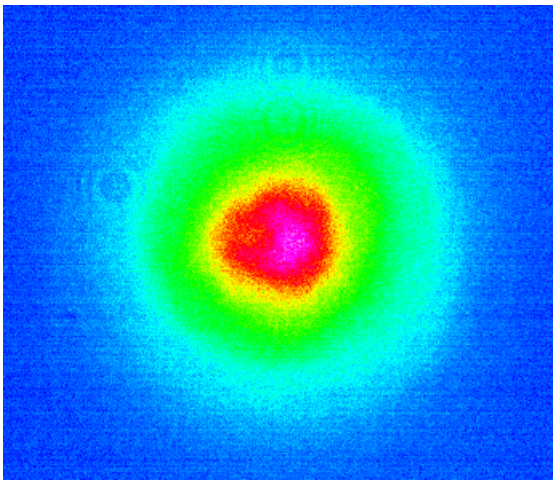

Figure 3.2: *A fundamental Gaussian beam. The intensity falls transversely of as a Gaussian function. The beam profiles in this chapters are measured in the setup of fig. 5.1.*

where A is a normalization constant and $q(z)$ and $p(z)$ are trial function dependent on the z-coordinate.

We can now solve the wave equation for a Gaussian mode, by inserting our ansatz in the paraxial wave equation and retrieving the full electric field form. For a Gaussian beam propagating in the z-direction and polarized in the x-direction, this results in [22]

$$\mathbf{E}^G = A\frac{w_o}{w(z)}e^{-\frac{x^2+y^2}{w(z)^2}}e^{i(kz-\omega t)}e^{\frac{ik(x^2+y^2)}{2R(z)}}e^{-i\varphi(z)}\hat{\mathbf{x}}, \tag{3.10}$$

with $A = \sqrt{\frac{2}{\pi}}$. Here the first part $A\frac{w_o}{w(z)}e^{-\frac{x^2+y^2}{w(z)^2}}$ is responsible for the amplitude of the Gaussian light field and the second part $e^{i(kz-\omega t)}e^{\frac{ik(x^2+y^2)}{2R(z)}}e^{-i\varphi(z)}\hat{\mathbf{x}}$ is responsible for the phase of the Gaussian light field. As can be seen, the phase of the Gaussian field is not dependent on the orbital angular momentum, since the phase is defined in the exponents and for a zero OAM $e^{i\ell\phi} = e^0 = 1$. Let us now define the terms in eq. 3.10 [22].

$w(z)$ is the beam spot. It is defined as the radius over which the transverse electric field falls of as $\frac{1}{e}$ for a plane z. If we define $z = 0$ at the focal point of the beam, we can define the beam waist as $w_0 = w(0)$. The Rayleigh range is defined as $z_R = \frac{\pi w_0^2}{\lambda}$, where λ is the wavelength of the beam. The Rayleigh range is the distance from the focal point in the z-direction for which the beam spot equals $w(z_R) = \sqrt{2}w_0$. For $z \gg z_R$ the

beam spot increases linearly as $w(z) = \frac{w_o z}{z_R}$.

In eq. 3.10 $e^{\frac{ik(x^2+y^2)}{2R(z)}}$ is the only phase term which depends on all coordinates. Therefore, this term corresponds to the curvature of the wavefronts. The denominator in the exponential contains the radius of curvature $R(z) = z(1 + \frac{z_R^2}{z^2})$. In the focal point $z = 0$ the radius of curvature $R(0) = \infty$. Hence in the focal point a Gaussian beam is described by a plane wave. At the Rayleigh range the radius of curvature is given by $R(z_R) = 2z_R$. The Rayleigh range can be seen as the border between ray and wave optics. At distances very far from the focal point ($|z| \gg z_R$) the light is traveling in straight lines from and toward the focal point and the radius of curvature is approximately $R \approx z$, while at distances between the focal point and the Rayleigh range the wave nature of light are surfacing.

The phase term in the last exponent $\varphi(z)$ is the Gouy phase. The Gouy phase is given by $\varphi = arctan(\frac{z}{z_R})$. It causes a phase shift of π between $z = -\infty$ and $z = \infty$, where the phase shift it contributes is most radically in the region near the focal point, i.e. in the region $-z_r < z < z_R$.

3.2.2 Higher-Order Gaussian Mode

The field of a paraxial beam can be decomposed by a mode expansion, where the zeroth order term is represented by the fundamental Gaussian mode. The higher order terms can be described in several orthonormal bases. Here we discuss two such bases: the Laguerre-Gauss basis $\{LG_p^\ell\}$ and the Hermite-Gauss basis $\{\mathrm{HG}_{\ell,p}\}$, where ℓ, p are the mode numbers.

Laguerre-Gauss Basis

We will first discuss the Laguerre-Gauss basis (fig. 3.3). The Laguerre-Gaussian modes can be used for a mode expansion in the cylindrical coordinate system (r, θ, z). The mode numbers ℓ, p in the Laguerre-Gaussian basis describe the azimuthal and the radial order of the mode respectively and the total order of the mode is given by $N = 2p + |\ell|$ [22]. As stated in section 3.1 the Laguerre-Gauss modes possess a nonzero orbital angular momentum. Hence it has helical wavefronts and the field of a Laguerre-Gauss mode of azimuthal order ℓ consists of photons with orbital angular momentum $\ell\hbar$.

Version of July 4, 2019– Created July 4, 2019 - 14:30

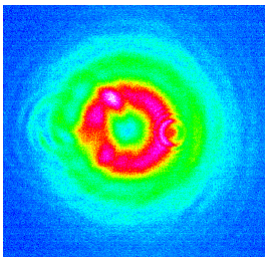

(a) *LG_0^1. First order Gaussian mode.*

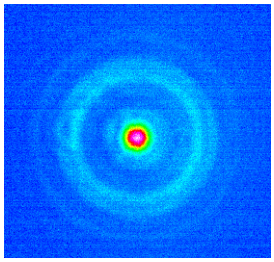

(b) *LG_1^0. Second order Gaussian mode.*

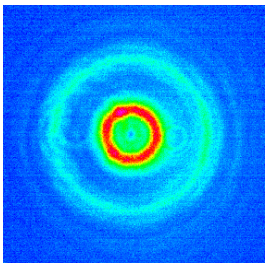

(c) *LG_1^1. Third order Gaussian mode.*

Figure 3.3: *Some examples of the beam profiles of Laguerre-Gauss modes.*

The field of the Laguerre-Gauss mode is given by [7]

$$LG_p^\ell = \sqrt{\frac{2p!}{\pi(p+|\ell|)!}} \frac{w_0}{w(z)} \left(\frac{r\sqrt{2}}{w(z)}\right)^\ell L_p^\ell \left(\frac{2r^2}{w(z)^2}\right) \cdot e^{-\frac{r^2}{w(z)^2}} e^{i(kz-\omega t)} e^{\frac{ikr^2}{2R(z)}} e^{i\ell\theta} e^{-i\varphi(z)}, \tag{3.11}$$

where $\{L_p^\ell(x)\}$ is the family of associated Laguerre polynomials. It can be checked that the zeroth order Laguerre-Gauss mode LG_0^0 returns to the fundamental Gaussian mode. The phase term $e^{i\ell\theta}$ is the phase due to the orbital angular momentum of the mode and causes the helical structure of the wavefronts.

Hermite-Gauss Basis

If we mode expand a paraxial beam in the Cartesian coordinate system (x, y, z), we can use the rectangular Hermite-Gauss modes (fig. 3.4). The mode numbers m, n of the Hermite-Gauss modes represent the horizontal (x-component) and vertical (y-component) order of the mode respectively and the total order of the mode is given by $N = m + n$ [22]. For the Hermite-Gauss modes the mode numbers are not associated with the orbital angular momentum. However the modes can possess orbital angular momentum.

The field of a Hermite-Gauss mode is given by [8]

$$HG_{m,n} = \sqrt{\frac{2^{1-N}}{\pi m!n!}} H_m\left(\frac{\sqrt{2}x}{w(z)}\right) H_n\left(\frac{\sqrt{2}y}{w(z)}\right) \cdot e^{-\frac{x^2+y^2}{w(z)^2}} e^{i(kz-\omega t)} e^{\frac{ik(x^2+y^2)}{2R(z)}} e^{-i\varphi(z)}, \tag{3.12}$$

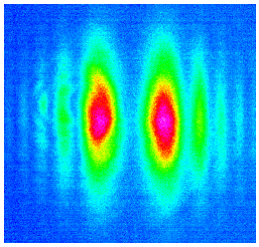

(a) *$HG_{1,0}$. First order Gaussian mode.*

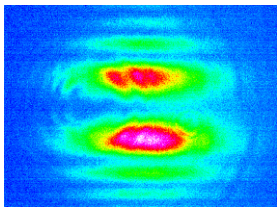

(b) *$HG_{0,1}$. First order Gaussian mode.*

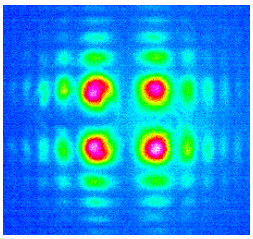

(c) *$HG_{1,1}$. Second order Gaussian mode.*

Figure 3.4: *Some examples of the beam profiles of Hermite-Gauss modes. The additional fringes shown in the pictures are due to the fact that s phase-only SLM can only make an approximation of the higher order modes. So these fringes on the sides are not real Hermite-Gauss modes.*

where $\{H_i\}$ is the family of Hermite polynomials. The zeroth order Hermite-Gauss mode $HG_{0,0}$ returns again to the fundamental Gaussian mode.

3.2.3 Spatial Light Modulator

In our experiment we use two spatial light modulators (SLM) to convert the Gaussian laser beam to the desired order modes. A SLM is a device, which can perform a spatially dependent modulation on a light beam. In our case we use a SLM, which only modulates the phase of the incoming light beam. The SLM can be connected to a computer, on which the desired modulation pattern can be selected. This pattern will then be displayed on a small screen (≈ 2 cm^2) of which the light beams will be reflected and the hologram modulates the phase of the light beam.

In our experiment we are mainly interested in the fundamental Gaussian mode (no modulation) and the first-order Laguerre-Gauss, Hermite-Gauss and 45°rotated Hermite-Gauss modes. For the Laguerre-Gauss and Hermite-Gauss modes, the SLM can only modulate them as an approximation. Besides selecting the modes the SLM can, with the use of the Zernike polynomials, also be used to modulate other aspects of the beam, such as spatial position, diameter and diagonalization. Last of all it is important to note that the effects of the SLM on the beams are wavelength dependent.

Chapter 4

Spontaneous Parametric Down-Conversion

In chapter 2 we have discussed the mathematical description of entangled states. However, it is not been stated how such states could arise experimentally. The most commonly used method to entangle photons is by spontaneous parametric down-conversion or SPDC [20]. SPDC is a second order nonlinear process [24]. It is realized in a nonlinear crystal*, where an incoming pump photon is split into two frequency down-converted photons, a signal and an idler photon (fig. 4.1). These signal and idler photons can among others be entangled in their polarization, angular momentum and frequency [25]. SPDC has no fundamental limit to the amount of entangled pairs generated. However, generation of increasing amounts of pairs requires an increase in the pump beam intensity [25]. With increasing pump beam intensities the problem arises that intensities beyond the damage threshold of the crystal are often required. In this chapter we restrict ourselves to SPDC in a type I crystal, where the signal and idler beams have the same polarization.

In SPDC, the combined energy and momentum of the signal and idler beams is equal to the energy and momentum of the pump beam [24], so

$$E_p = E_s + E_i, \quad \vec{p}_p = \vec{p}_s + \vec{p}_i, \tag{4.1}$$

where p, s, i denote the pump, signal and idler beam respectively. In order to generate entangled photons with a high efficiency, it is required that the the signal and idler beams generated in the crystal interfere constructively at the output interface of the crystal. Therefore the phase mismatch $\Delta\mathbf{k}L$

*In our experiment we use a PPKTP crystal

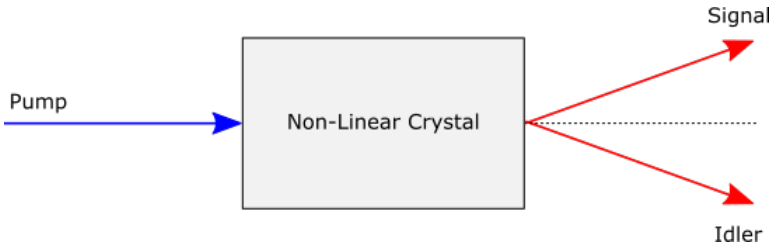

Figure 4.1: *The process of SPDC. A pump photon (413.1 nm) is focused into a nonlinear crystal, where it is split, due to spontaneous parametric down conversion, into a signal and a idler photons (both 826.2 nm).*

(fig. 4.2), where **k** is the wave vector and L is the length of the crystal, is an very important quantity in the process of SPDC. The signal and idler beams will interfere constructively during their propagation paths when [20]

$$\Delta k_z L = (k_{p,z} - k_{s,z} - k_{i,z})L = 0 \tag{4.2}$$

The procedure to dissolve this phase mismatch is simply called phase matching.

4.1 Phase Matching

In SPDC, the photon energy of the pump beam $\hbar\omega_p$ is the sum of the photon energies of the signal and idler beams. So, we have the frequency relation [20]

$$\omega_p = \omega_s + \omega_i, \tag{4.3}$$

Further as given in eq. 4.2, the phase mismatch of the SPDC photons depends on the difference between the z-components of the wave vector of the pump beam and the combined wave vector of the signal and idler

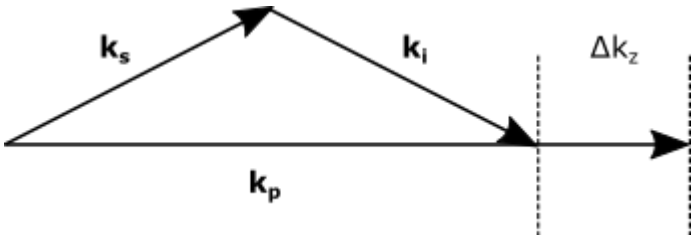

Figure 4.2: *A phase mismatch Δk_z is shown between the wave vector of the pump photon and the combined wave vector of the signal and idler photons. The efficiency of the SPDC process is maximized if $\Delta k_z = 0$ (phase matched).*

beams. Since the dispersion relation of the refractive index of a nonlinear crystal depends on the frequency of the passing photons, i.e. $n(\omega_k, T) \neq n(\omega_l, T)$ for $\omega_k \neq \omega_l$, Δk_Z can be written as

$$\Delta k_z = \frac{2}{c}(\omega_p n(\omega_p, T) - \omega_s n(\omega_s, T) - \omega_i n(\omega_i, T)), \tag{4.4}$$

Δk_z has in general a nonzero value. Therefore a phase mismatch arises and the signal and idler beams will not interfere constructively. Hence, we call $\Delta k_z = 0$ the phase matching condition. In order to tell if the signal and idler photons are phase matched we look at the intensity of the SPDC field. Since the intensity of the SPDC field is given by [20]

$$I \propto \frac{sin^2(\frac{1}{2}\Delta k_z L)}{(\frac{1}{2}\Delta k_z L)^2} L^2, \tag{4.5}$$

we see that the phase matching condition is satisfied, when the intensity of the SPDC field is maximized. In our experiment we work with a KTP crystal and a pump beam of wavelength $\lambda = 413.1$ nm. Ordinary phase matching procedures do not work for a combination of a KTP and this pump beam wavelength [24]. Therefore we use a KTP crystal which is periodically poled and the phase matching procedure we use is called quasi-phase matching.

4.1.1 Quasi-Phase Matching

From eq. 4.5 we know, that for a phase mismatch, a coherence length $l_c = \frac{\pi}{\Delta k_z}$ exists over which the signal and idler photons built up a phase difference of π. In a periodically poled crystal a periodic structure of poling period $\Lambda = 2l_c$ is introduced, which changes the sign of the nonlinear coefficient [24]. This also adds a phase difference of π over every coherence length, canceling the effects of the initial phase built-up. The periodic structure introduces an additional term in the phase match condition, dependent on the poling period. The modified phase matching condition then becomes [25]

$$\Delta k_z' = \Delta k_z - \frac{2\pi}{\Lambda} = 0 \tag{4.6}$$

For a periodically poled crystal, the intensity of the SPDC field becomes

$$I \propto \frac{sin^2(\frac{1}{2}(\Delta k_z - \frac{2\pi}{\Lambda})L)}{(\frac{1}{2}(\Delta k_z - \frac{2\pi}{\Lambda})L)^2} L^2, \tag{4.7}$$

This shows, that the phase matching condition still agrees with a maximized intensity of the SPDC field. A nice chart of the intensity against the longitudinal direction of the crystal for different Δk_z can be found in [24, fig. 1.3]. Now in order to phase match the signal and idler photons, we have to alter their wave vectors to match the phase matching condition. Since the wave vectors can be written as a function of the refractive index of the crystal and the refractive index depends on the temperature of the crystal [26], the phase matching condition can be satisfied by tuning the temperature of the crystal. So the appropriate temperature of the crystal is the temperature that maximizes the intensity of the SPDC field.

4.2 The SPDC-Hamiltonian

Let us now give a quantum description of the process of SPDC. In this description we denote photon states by $|n_k\rangle$, where k is the mode of the photons and n the number of photons in that particular mode. Note that in this formulation a state $|n_k\rangle$, where $n \neq 0, 1$, represents a composite state of the occupied photon states, i.e. $|n_k\rangle = |1_k\rangle_1 \otimes \cdots \otimes |1_k\rangle_n$ for $n \neq 0, 1$. We first define two operators. The annihilation operator $\hat{a}_l$ and the photon creation operator $\hat{a}_l^\dagger$, which we define as [5]

$$\hat{a}_l |1_l\rangle = |vac\rangle , \tag{4.8a}$$

$$\hat{a}_l^\dagger |vac\rangle = |1_l\rangle , \tag{4.8b}$$

where in eq. 4.8a a single photon in mode l is annihilated leaving behind the vacuum state $|vac\rangle$ and in eq. 4.8b a single photon in mode l is generated from the vacuum state. The creation and annihilation operators are in fact equivalent to the ladder operators $\hat{a}_+, \hat{a}_-$ of the harmonic oscillator, respectively. With the use of these operators the Hamiltonian for SPDC can be constructed. This results in [5]

$$\hat{H}_{SPDC} = i\hbar\kappa(\hat{a}_p^\dagger \hat{a}_s \hat{a}_i e^{i\Delta\mathbf{k}\cdot\mathbf{r} - i\Delta\omega t} + \hat{a}_p \hat{a}_s^\dagger \hat{a}_i^\dagger e^{-i\Delta\mathbf{k}\cdot\mathbf{r} + i\Delta\omega t}), \tag{4.9}$$

where the first term accounts for the processes of SFG[†] or SHG[‡] and the second term accounts for the process of SPDC itself. Further κ is defined as the strength of the nonlinear interaction. Our experiment is focused on four-photon states entangled in their orbital angular momentum (OAM) degrees of freedom. In order to describe this type of entanglement due to

[†]Sum-Frequency Generation.
[‡]Second-Harmonic Generation.

SPDC, the Hamiltonian for SPDC has to be rewritten in OAM space. For a Gaussian pump beam and a rotational symmetric crystal this results in the Hamiltonian [3]

$$\hat{H} = \sum_{\ell=-\infty}^{\infty} \frac{1}{2} i\kappa\hbar(\hat{a}_{\ell}^{\dagger}\hat{a}_{\bar{\ell}}^{\dagger} - \hat{a}_{\ell}\hat{a}_{\bar{\ell}}), \tag{4.10}$$

where ℓ is the quantum number for orbital angular momentum. When we let this Hamiltonian work on the state $|0\rangle$, this results in the state

$$|\Psi\rangle = e^{-i\frac{\hat{H}t}{\hbar}} |0\rangle \tag{4.11}$$

We can now Taylor expand this state, which we will do to second order, since we are interested in up to four-fold entangled states. The Taylor expansion gives

$$|\Psi\rangle = e^{-i\frac{\hat{H}t}{\hbar}} |0\rangle \approx (\mathbb{1} - \frac{it}{\hbar}\hat{H} - \frac{t^2}{2\hbar^2}\hat{H}^2) |0\rangle \tag{4.12}$$

In this Taylor expansion, the first order term will generate a state $|\Psi_2\rangle$ consisting of single entangled photon pairs, according to [24]

$$|\Psi_2\rangle = \gamma \sum_{\ell=1}^{\infty} |1_{\ell}, 1_{\bar{\ell}}\rangle , \tag{4.13}$$

where $\gamma \propto \kappa t$ depends linearly on the pump beam intensity and in which all OAM modes which are not occupied by a photon are left out of the summation. The second order of the Taylor expansion is responsible for the generation of the state $|\Psi_4\rangle$, which is a four-photon state containing all occupied double pairs. The double pair state results in [24]

$$|\Psi_4\rangle \propto \gamma^2 \left(\sum_{i,j=1, i\neq j}^{\infty} \left| 1_{\ell_i}, 1_{\ell_j}, 1_{\bar{\ell}_i}, 1_{\bar{\ell}_j} \right\rangle + 2 \sum_{\ell=1}^{\infty} |2_{\ell}, 2_{\bar{\ell}}\rangle \right) \tag{4.14}$$

In this state the first term, where two photon pairs with different orbital angular momentum are generated, corresponds to process where both photon pairs are created spontaneous and the two photon pairs mutually uncorrelated. The second term, where two identical photon pairs are generated, corresponds to a stimulated creation process, which generates the second photon pair as a perfect clone of the first pair

By the entanglement definitions given in section 2.4 we see that the states $|\Psi_2\rangle$ and $|\Psi_4\rangle$ are indeed entangled two-photon and four-photon states, respectively.

Version of July 4, 2019– Created July 4, 2019 - 14:30

Chapter 5

Experiment

The goal of our experiment is to generate entangled four-photon states and make attempts of measuring the entanglement features in their OAM degrees of freedom. We use pulsed spontaneous parametric down-conversion (SPDC) in a type-1 PPKTP* crystal to generate the entangled four-photon states. The SPDC photons are separated by use of three beam splitters and via spatial light modulators (SLM) imaged onto four single mode fibers. Single photon counters and a multi-channel time tagging computer card is used to measure the coincidence rates of the incoming photons. By changing the holograms on the SLMs we can analyze the entanglement properties of the OAM mode space of the four-photon space.

For this project we rebuilt a former preliminary experiment [3]. Our motivation for doing this was to improve the stability of the setup, since before this was insufficient to determine some characteristics of the measured entangled states. We mainly improved the stability by decreasing the size of the setup to fit on a single optical breadboard.

We will start with giving a full description of the experimental setup (fig. 5.1), hereafter we will lay out the alignment procedure to ease future explorations of the experiment.

5.1 Setup

We use a pulsed Ti:Sapphire laser as pump laser. The laser emits 826.2 nm pulses with a pulse length of $\Delta t = 2$ ps and a pulse frequency of $f_p = 80$ MHz. The pump beam is frequency doubled to 413.1 nm by sum-frequency generation (SFG) in a LBO crystal. Before entering the setup the

*Periodically Poled Potassium Titanyl Phosphate.

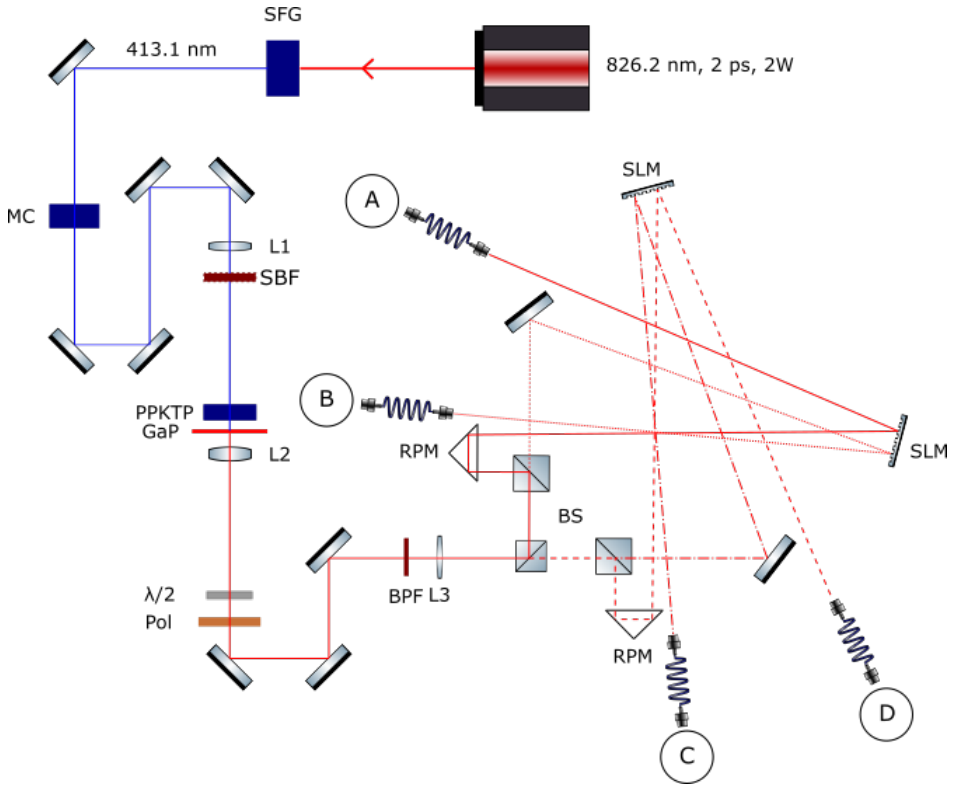

Figure 5.1: *A picosecond pulsed pump beam is frequency doubled by sum-frequency generation (SFG) and mode cleaned (MC). Then the pump beam is focused (L1) on the PPKTP crystal. The SPDC photons are separated with beam splitters in distributed in four downconverted beams. The SPDC light is 4f-imaged (L2 and L3) on the SLMs. The holograms of the SLM can be changed to select the desired modes. Finally the beams are far-field imaged on the single mode fibers which are connected to the single photon counters.*

pump beam propagates through some optical elements in order to mode clean the beam to its Gaussian form. We wanted to fit the entire setup onto a single optical table to guarantee its stability. Therefore we minimized the area the setup covers to fit on an optical breadboard of 75×85 cm^2.

When entering the breadboard we focus the pump beam into a 2 mm long PPKTP crystal with lens L1 ($f = 25$ cm) and a single band-pass filter (SBF) is used to remove the residual 826.2 nm laser light. Inside the crystal the pump beam is converted into the desired SPDC light of 826.2 nm, which contains the entangled photons, due the nonlinearity of the crystal. The SPDC light is phase-matched by periodic poling of the crystal and utilizing the temperature dependence of the refractive index of the crystal. The crystal is heated to a temperature of $T \approx 61°$C in order to reach the

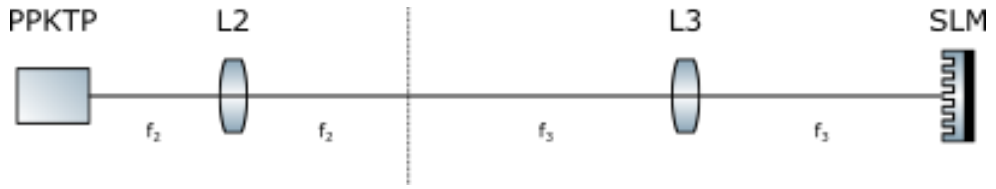

Figure 5.2: *A 4f-image is an imaging technique which magnifies the imaged object, according to $M = \frac{f_3}{f_2}$. The distances in a 4f-image setup are important and have to be distributed according to the figure. In our setup L2 has a focal length of $f_2 = 4$ cm and L3 has a focal length of $f_3 = 75$ cm, which result in a magnification of $M = 18.75$ cm.*

phase-match criterion. Behind the crystal we place a GaP-filter to filter out the residual 413.1 nm pump beam and a 826.2 nm band-pass filter (BPF) is used to filter out all the unwanted SPDC light. At 4 cm from the crystal we place the lens L2 ($f = 4$ cm). Together lenses L2 and L3 ($f = 75$ cm) work as a telescope, making a 4f-image of the SPDC light onto the SLMs (fig. 5.2). This results in a magnification of $M = \frac{75}{4} = 18.75$. The pump photons are horizontally polarized and we use type I SPDC which will convert the signal and idler beams to a vertical polarization. However the SLM holograms only work on a horizontal polarization Therefore we have to rotate the polarization of the SPDC light by 90°. We do this by placing a half-wave plate between L2 and L3, making an angle of 45°with respect to the horizontal polarization of the pump beam. The half-wave plate ($\lambda/2$) is then followed by a polarizer (Pol) which filters out the residual horizontal polarized light. Behind the lens L3 three nonpolarizing beam splitters (BS) spatially separate the four down-converted light beams from each other. For two of the four beams right-angle prism mirrors (RPM) are used to equalize the optical path length of the four down-converted beams. We align two beams per SLM, one on the left of each SLM-display (beam A and C) and one on the right of each SLM-display (beam B and D). To make the setup fit in the available area we found that beams A and D should make an angle of incidence of $\theta_{A,D} \approx 10°$at the display of the SLM and beams B and C should make an angle of incidence of $\theta_{B,C} \approx 5°$. With the holograms of the SLMs we can select the desired mode, which are the zeroth order Gaussian mode and the first order modes. We can also select the basis of the first order modes in which we want to measure the entangled photons. For the first order mode we look at the Laguerre-Gauss basis $\{\mathrm{LG}_0^{+1}, \mathrm{LG}_0^{-1}\}$ and the Hermite-Gauss basis $\{\mathrm{HG}_{0,1}, \mathrm{HG}_{1,0}\}$. Via the SLMs the beams are far-field imaged onto the single mode fibers which are connected to the single photon counters. Here we can record single count

rates for all detectors, as well as 2,3 and 4 fold coincidences for all detector combinations. We use projective measurements to investigate the OAM mode space and appropriate entanglement witnesses can be used to check if the photons of the measured coincidences show entanglement features [3].

5.2 Alignment Procedure

In this section we give an overview of the alignment procedure used. In this alignment procedure we make use of the 413.1 nm pulsed pump laser (at only a few mW power) and 826.2 nm alignment beams from a laser diode connected to the single mode fibers. As master alignment beam we used beam A, since this beam has the least degrees of freedom in its optical path and is therefore the hardest to align.

First it is important to equalize the heights of the single mode fibers, in order that all beams can travel through the setup with ideally no vertical displacement and the optical path lengths remain the same. This can be done by placing a camera in front of the fiber of beam A and measuring its height. The height of beam A has to be set to match the height of the display of the SLM, since this is the only element in the setup with a fixed height. By placing the camera in front of the other fibers their heights can be matched to the master beam. Further we make sure the beams experience no significant vertical displacement through out the setup, which can be best done by moving the camera through the setup while adjusting the optical elements where vertical displacement of the beams is observed. Also one should take care that right angles are made by the beams in the beams splitters and at the mirrors as in fig. 5.1, this will highly ease the alignment effort and can best be done with use of two pinholes aligned on the same path. This will already roughly align the four alignment beams. The two pinholes, separated at a large distance, can also be used to roughly align the pump beam on the master alignment beam. The alignment of the pump beam can best be done before placing the crystal and the lenses in the setup, on accounts of the effects a phase mismatch in the crystal could cause. A small misalignment of the pump beam onto the single mode fiber of the master alignment beam would be optimal, because of the difference of wavelength of the pump beam and the SPDC light.

Lens Alignment and Crystal Position

For the alignment of the lenses we start with L3. It is beneficial to measure the focal length of the lens first, since this can slightly differ from the given $f = 75$ cm. We measure the focal length by pointing an alignment beam at L3, we place a camera behind L3 and move the camera until it is in the focus. By measuring the distance between the camera and L3 we find the focal length of the lens (take into account the distance between the case of the camera and the CCD chip). We place L3 at a distance to the SLM equal to the determined focal length of L3. The x, y-position of the lens can be aligned by measuring the beam position of the alignment beam without the lens first. We place back L3 and change the x, y-position, using an x, y-stage, until the alignment beam arrives at the camera at exactly the same position as it did without L3. Since we want to make a 4f-image of the SPDC photons at the crystal on the SLMs, we have to place L2 in front of L3 at a distance that is the sum of their focal lengths, i.e. $\Delta x = f_2 + f_3$. In order to do so, we determine the focus position of L3 near where we want to place L2, which can be done again by moving a camera until the alignment beam is in its focal point. Now instead of the alignment beam we will use the pump beam to align L2. We rotate the camera to detect the pump beam. Since the camera still has to be in the focal point of L2, we again have to take into account the position of the CCD chip inside the camera, since that is what has to stay on the same position. We measure the position of the pump beam and place L2 in the path of the pump beam. We move L2 along the path of the pump beam until the pump beam is focused, possibly with the use of an x, y, z-stage. Then we can adjust the x, y-position of L2 until we measure the same beam position at the camera as without L2. After attaching L2 to the breadboard we also determine the position of its focal point from the other side, using again the alignment beam, with the camera in the same manner as we did before for L3. We note this as the position where the PPKTP crystal has to be staged. For the alignment of L1 we want to detect the pump beam, so we have to rotate the camera again in a way that the position of the CCD chip remains unchanged. With the help of an x, y, z-stage we can align L1 in the same manner as we did for L2.

When all lenses are aligned, we place the PPKTP crystal on a x, y-stage at the determined position. We place a red LED next to L2 outside the setup and we focus the LED light with another lens ($f = 4$ cm) on the crystal, such that the crystal is illuminated. Via a flip-mirror (FM) a 4f-image is made of the reflection of the crystal on a CCD camera outside the setup, using L2 and a lens ($f = 10$ cm) on a focal distance from the camera

(fig. 5.3). By this 4f-image we can look at the whole crystal (we will only see the edges, since it is anti-reflection coated). We probably have to adjust the focus of L2 slightly, due to inaccuracy of placing the crystal, which can be done with the z-component of the x, y, z-stage. We alter the x, y-position of the crystal such that the pump beam is passing through the crystal far enough from the edges, which can be seen on the 4f-image of the reflection of the crystal. The z-position of L1 should be altered slightly to focus the pump beam perfectly at the crystal. We also look at the 4f-image of the reflection of the alignment beam on the crystal to see if it is indeed aligned with the pump beam (fig. 5.4).

When the crystal is placed and the beams are nicely focused onto the crystal we set the GaP-filter in place behind the crystal. Now it is time to let the crystal reach its phase-matching conditions. We will phase-match the SPDC light by controlling the temperature of the crystal, for which we use a PID temperature controller. From eq. 4.7) we know that the phase-matching conditions are met, when the peak intensity of the SPDC light reaches a maximum. Hence, by measuring the peak intensity of the SPDC light with a camera and changing the temperature of the crystal, we found a maximum peak intensity at $T_{crys} = 61°\text{C}$ (fig. 5.5b).

Near and Far Field Image

All optical elements are set up, therefore it is time to align the alignment beams more accurately onto each other. We do this by still taking beam A as the master alignment beam on which we align beams B, C and D.

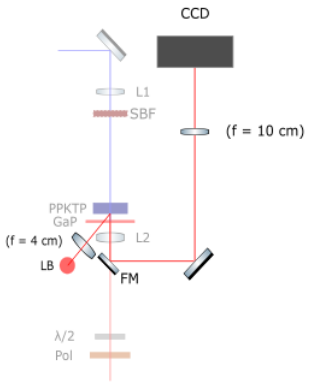

Figure 5.3: *A zoom-in of the setup is shown (with some alterations). A flip mirror interrupts the beam path and via a lens ($f = 10$ cm) a 4f-image of the surface of the crystal is made.*

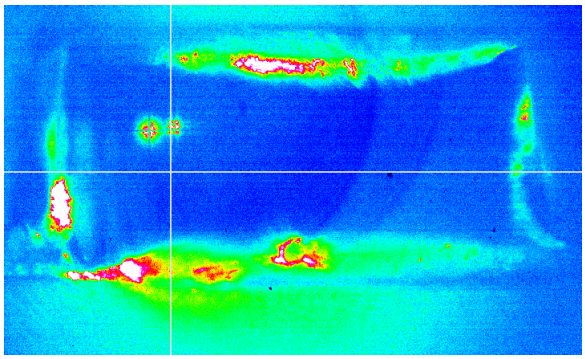

Figure 5.4: *A 4f-image of the reflection of the crystal. The alignment beam is aligned on the crystal in a Hermite-Gauss mode. The two Hermite-Gauss spots are actually from the same beam. The left one is probably a reflection effect.*

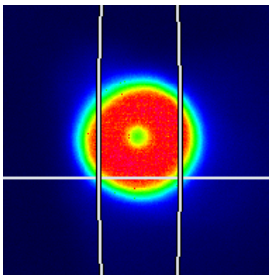

(a) *SPDC light at crystal temperature $T_{crys} = 44°C$. The phase-matching conditions are not met. The wave vectors of the SPDC photons are not matched, which causes the peak intensity to be dislocated from the center (donut shape).*

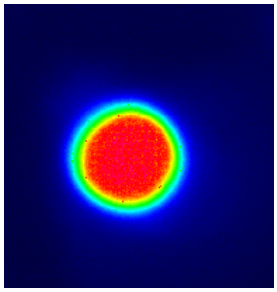

(b) *SPDC light at crystal temperature $T_{crys} = 61°C$. The peak intensity is maximized and the donut shape has disappeared. Therefore the phase-matching conditions are met.*

In order to do this we use a near and far field image. To make such an image we put two flip mirrors between L2 and L3, where the first flip mirror transmits a part of the alignment beams to the second flip mirror and reflects a part to a camera outside the setup. The camera is placed in the focal point of L3, so that the alignment beams are focused by L3 on the camera to make a near field image. The second flip mirror reflects the residual part of the alignment beams through another lens ($f = 50$ cm) which makes a far field image on the camera (fig. 5.6). The near and far fields are best observed in the Hermite-Gauss mode, which are therefore selected by the SLMs. Now we can align the alignment beams one by one on the master beam A. To do this we first align the far field image by only using the optical element the alignment beams pass before they

enter the first beam splitter. When the far field image is aligned, we start with the near field image. The near field image can be aligned by only changing the coefficients of the first and second order Zernike polynomials on the SLM, which represent vertical and horizontal displacement of the beam respectively. Changing the Zernike polynomials will not affect the far field image, which is therefore still aligned. When all alignment beams are aligned, they should also all be roughly aligned with the pump beam, since we have done that already for the master alignment beam.

Optimization of Coincidence Counts

Since the pump beam is roughly focused onto all four single mode fibers, we can connect the single mode fibers to the photon counters and we should already measure some photon counts and possibly even some coincidence counts. It is now a matter of optimizing the photon and coincidence counts. This can be done by changing the optical path of the pump beam slightly or changing the coefficients of the Zernike polynomials. We start with changing the Zernike polynomials. In the software we used to analyze the photon and coincidence counts, optimization of the Zernike coefficients was automated. It iterates over a range of values for one of the Zernike polynomials to find the value which maximizes the coincidence counts. This has to be done for every Zernike coefficients and for all beams separately. After optimizing the Zernike coefficients the near field image of the alignment beams will be misaligned again. This has to be re-aligned, by changing the position of all alignment beams, i.e. including master beam, to the average position of all four alignment beams. To do

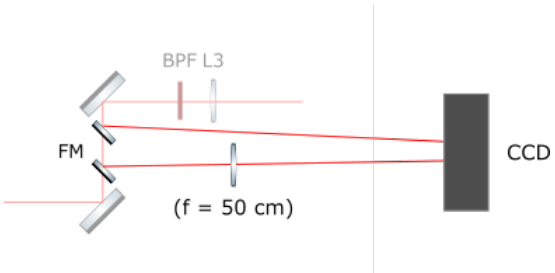

Figure 5.6: *A zoom-in of the setup, where the alignment setup for the near and far field image is shown. Two flip mirrors (FM) interrupt the beam path of the alignment beams and align the beams on the CCD camera, where a near and far field image is obtained. To obtain a far field image a lens ($f = 50$ cm) is used for the lower beam path.*

this we can again change the coefficients of the Zernike polynomials. This procedure will highly increase the coincidence counts, however probably it has to be even further optimized. To optimize the coincidence counts further we slightly change the direction and position of optical elements in the setup. Alterations that are likely to effectively increase the coincidence counts, are changes of the x, y-position of the crystal, the focus of the lenses and applying a slight beam walk with the mirrors. Changing the temperature of the crystal can also increase the coincidence counts, since the phase matching condition is possibly not perfectly met. In fact the optimization of the coincidence counts is quite a matter of trial and error and alterations may depend on alterations of other elements, therefore we have to repeat this procedure many times. Eventually the photon counts should roughly approach $n_{pc} = 10^6\ \mathrm{s}^{-1}$ and the coincidence counts should be around 10% of the photon counts.

5.3 First Results

Unfortunately the time span of this project turned out to be insufficient to fully complete the experiment and to sufficiently measure and analyze the entangled four-photon states. However we will state and discuss our experimental accomplishment and our first results, which already indicate that entanglement features of the generated photon states can be observed by this experiment.

5.3.1 First Results and Discussion

In our attempt to explore the entanglement features of four-photon OAM states, we built a setup where four-photon states were generated by SPDC in a PPKTP crystal. We succeeded to decrease the area taken by the setup with respect to a former similar setup [3]. We have decreased the area in order to fit the setup on a single optical table to increase the stability of the setup. Eventually we have decreased the size of the setup to an area of $75 \times 85\ \mathrm{cm}^2$ and we have built the setup on a portable optical breadboard of comparable size. We managed to do this by using lenses (L2 and L3) of shorter focal length with respect to former research [3]. In this former research lenses L2 and L3 have been used with respectively $f_2 = 5$ cm and $f_3 = 100$ cm, whereas we have used lenses of $f_2 = 4$ cm and $f_3 = 75$ cm respectively. We chosen these focal lengths in order to obtain a comparable ratio between the lenses, which results in a comparable magnification of the 4f-image of the SPDC light onto the SLMs. Where possible, we built

the setup in a way that the corners in the optical paths of the light beams make right angles. This is done to ease the alignment procedure, since this decreases the mutual dependencies of the degrees of freedom in the setup.

We also developed and applied an alignment procedure as described in section 5.2, which is in our opinion an efficient and successful way to handle the alignment of this experiment. An optimal alignment procedure for this experiment is of great importance, since with respect to two-photon entanglement, four-photon entanglement requires highly increasing experimental accuracy.

Further during this project, the software, responsible for measuring the photon and coincidence counts of the incoming photons, is improved. The details of the software and its improvements are not discussed in this thesis, for a discussion about the software another thesis about this experiment can be consulted [27].

In order to optimize the alignment of the setup we have mainly focused on the photon and coincidence counts of beam paths A and B (fig. 5.1). For these beam paths we have managed to measure photon counts up to $n_p = 3 \cdot 10^5$ s^{-1} and we have measured two-photon coincidence counts between these beam paths of $n_c = 1.8 \cdot 10^3$ s^{-1}. These counts are still far to low to obtain significant data about the entanglement features. Ideally photon counts of approximately $n_p \approx 10^6$ s^{-1} should be obtained with coincidence rates of around a factor 10 less. Unfortunately we lacked the time to complete the optimization process of the alignment. However, first indications of the OAM entanglement features have been measured

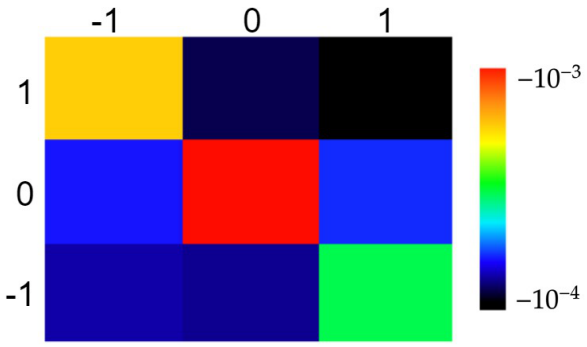

Figure 5.7: *First correlation measurement of the photon coincidences between channel A and B for the zeroth and first order OAM. The axes denote the OAM orders of channel A and B and the coincidences are given as a ratio of the photon counts.*

for these coincidences between A and B. In the photon coincidences of the two incoming beams we measured correlations in both the zeroth and first order of the orbital angular momentum. These correlations have been shown in fig. 5.7. Here the x-axis shows the zeroth and first order of the OAM $\ell = -1, 0, 1$ of the photons from channel A and the y-axis shows the zeroth and first order of the OAM $\ell = -1, 0, 1$ of the photons from channel B. And the coincidences are given as fractions of the photon counts. As can be seen correlations in the zeroth and first order OAM states have been observed. Here $\ell_A = 0$ is correlated to $\ell_B = 0$ and $\ell_A = \pm 1$ is correlated to $\ell_B = \mp 1$.

5.3.2 Conclusion

To explore the OAM entanglement features of the four-photon states we still have to highly increase the coincidence counts and the correlations measured still have to be obtained for several different bases to exclude the possibility of classical correlations. Further correlations for higher order OAM modes have to be obtained to be able to differentiate the spontaneous and stimulated terms in the four-photon entangled state (eq. 4.14). But the correlations measured do suggest entanglement features and therefore they are an indication that this experiment can be exploited to explore multipartite entanglement features in high-dimensional Hilbert spaces.

Bibliography

[1] Einstein, A.; Podolsky, B.; Rosen, N. (1935). *Can Quantum-Mechanical Description of Physical Reality Be Considered Complete?* Physical Review 47, 777–780. https://doi.org/10.1103/PhysRev.47.777

[2] Zhong, H. et al. (2018) *12-Photon Entanglement and Scalable Scattershot Boson Sampling with Optimal Entangled-Photon Pairs from Parametric Down-Conversion*. Physical Review Letters, 121(25), p. 250505. doi: 10.1103/PhysRevLett.121.250505.

[3] Hiesmayr, B.C.; de Dood, M.J.A.; Löffler, W. (2016). *Observation of Four-Photon Orbital Angular Momentum Entanglement*. Physical Review Letters 116. https://doi.org/10.1103/PhysRevLett.116.073601

[4] Malik, M. et al. (2016) *Multi-photon entanglement in high dimensions*, Nature Photonics. Nature Publishing Group, 10(4), pp. 248–252. doi: 10.1038/nphoton.2016.12.

[5] Couteau, C. (2018). *Spontaneous parametric down-conversion*. Contemporary Physics 59, 291–304. https://doi.org/10.1080/00107514.2018.1488463

[6] Hong, C.K.; Mandel, L. (1985). *Theory of parametric frequency down conversion of light*. Physical Review A 31, 2409–2418. https://doi.org/10.1103/PhysRevA.31.2409

[7] Allen, L.; Beijersbergen, M.W.; Spreeuw, R.J.C.; Woerdman, J.P. (1992). *Orbital angular momentum of light and the transformation of Laguerre-Gaussian laser modes*. Physical Review A 45, 8185–8189. https://doi.org/10.1103/PhysRevA.45.8185

[8] Beijersbergen, M.W.; Allen, L.; van der Veen, H.E.L.O.; Woerdman, J.P. (1993). *Astigmatic laser mode converters and transfer of orbital angular momentum*. Optics Communications 96, 123–132. https://doi.org/10.1016/0030-4018(93)90535-D

[9] Padgett, M.J.; Courtial, J. (1999) *Poincaré-sphere equivalent for light beams containing orbital angular momentum*. Opt. Lett. 24, 430–432

[10] Genovese, M. (2016). *Real applications of quantum imaging*. Journal of Optics 18, 073002. https://doi.org/10.1088/2040-8978/18/7/073002

[11] Strekalov, D.V; Sergienko, A.V.; Klyshko, D.N.; Shih, Y.H. (1995). *Observation of Two-Photon Ghost Interference and Diffraction*. Physical Review Letters 74, 4. https://doi.org/10.1103/PhysRevLett.74.3600

[12] Hillery, M.; Bužek, V.; Berthiaume, A. (1999). *Quantum secret sharing*. Physical Review A 59, 1829–1834. https://doi.org/10.1103/PhysRevA.59.1829

[13] Yu, I. C.; Lin, F. L.; Huang, C. Y. (2008). *Quantum secret sharing with multilevel mutually (un)biased bases*. Physical Review A 78. https://doi.org/10.1103/PhysRevA.78.012344

[14] Audretsch, J. (2007). *Entangled Systems: New Directions in Quantum Physics*, 1st ed. Wiley. https://doi.org/10.1002/9783527619153

[15] Debnath, L.; Mikusiński, P. (2005). *Hilbert spaces with applications*. 3rd. ed. ed. Elsevier Academic Press, Amsterdam; Boston.

[16] *The Double-Slit Experiment Cracked Reality Wide Open.* [WWW Document], n.d. URL https://curiosity.com/topics/the-double-slit-experiment-cracked-reality-wide-open-curiosity/ (accessed 6.19.19).

[17] Brandao, F.G.S.L.; Christandl, M.; Harrow, A.W.; Walter, M. (2016). *The Mathematics of Entanglement.* arXiv:1604.01790 [math-ph, physics:quant-ph].

[18] Mintert, F.; Viviescas, C.; Buchleitner, A. (2009). *Basic Concepts of Entangled States*, in: Buchleitner, A.; Viviescas, C.; Tiersch, M. (2009). *Entanglement and Decoherence*. Springer Berlin Heidelberg, Berlin, Heidelberg, pp. 61–86. https://doi.org/10.1007/978-3-540-88169-8_2

[19] Walter, M.; Gross, D.; Eisert, J. (2016). *Multi-partite entanglement*. arXiv:1612.02437 [cond-mat, physics:math-ph, physics:quant-ph].

[20] Pors, J. B. (2011). *Entangling Light in High Dimensions*. Doctoral Thesis, Leiden University

[21] Allen, L.; Padgett, M. (2011). *The Orbital Angular Momentum of Light: An Introduction*. in: Torres, J.P.; Torner, L. (2011). *Twisted Photons*. Wiley-VCH Verlag GmbH & Co. KGaA, Weinheim, Germany, pp. 1–12. https://doi.org/10.1002/9783527635368.ch1

[22] Galvez, E. J. (2009). *Gaussian Beams*. Department of Physics and Astronomy, Colgate University

[23] Pampaloni, F.; Enderlein, J. (2004). *Gaussian, Hermite-Gaussian, and Laguerre-Gaussian beams: A primer*. https://arxiv.org/abs/physics/0410021v1

[24] Yorulmaz, S. Ç. (2014). *Beyond photon pairs*. Doctoral Thesis, Leiden University

[25] Sabharwal, S. (2017). *Spatial Bunching of Entangled Four Photons*. MSc. Thesis, Leiden University

[26] Emanueli, S.; Arie, A. (2003). *Temperature-Dependent Dispersion Equations for KTiOPO4 and KTiOAsO4*. Applied Optics 42, 6661. https://doi.org/10.1364/AO.42.006661

[27] Lepides, A. (2019). *On Quadripartite Entanglement in High-Dimensional Hilbert Space.* BSc. Thesis, Leiden University